A Monte Carlo based method to estimate radiation dose from multidetector CT (MDCT): cylindrical and anthropomorphic phantoms

2005 Phys. Med. Biol. 50 3989

(http://iopscience.iop.org/0031-9155/50/17/005)

INSTITUTE OF PHYSICS PUBLISHING PHYSICS IN MEDICINE AND BIOLOGY

Phys. Med. Biol. **50** (2005) 3989–4004 doi:10.1088/0031-9155/50/17/005

A Monte Carlo based method to estimate radiation dose from multidetector CT (MDCT): cylindrical and anthropomorphic phantoms

J J DeMarco[1], C H Cagnon[1], D D Cody[2], D M Stevens[2], C H McCollough[3], J O'Daniel[2] and M F McNitt-Gray[1]

[1] David Geffen School of Medicine at UCLA, Los Angeles, CA, USA
[2] UTMD Anderson Cancer Center, Houston, TX, USA
[3] Mayo Clinic, Rochester, MN, USA

Received 5 April 2005, in final form 15 June 2005
Published 11 August 2005
Online at stacks.iop.org/PMB/50/3989

Abstract

The purpose of this work was to extend the verification of Monte Carlo based methods for estimating radiation dose in computed tomography (CT) exams beyond a single CT scanner to a multidetector CT (MDCT) scanner, and from cylindrical CTDI phantom measurements to both cylindrical and physical anthropomorphic phantoms. Both cylindrical and physical anthropomorphic phantoms were scanned on an MDCT under the specified conditions. A pencil ionization chamber was used to record exposure for the cylindrical phantom, while MOSFET (metal oxide semiconductor field effect transistor) detectors were used to record exposure at the surface of the anthropomorphic phantom. Reference measurements were made in air at isocentre using the pencil ionization chamber under the specified conditions. Detailed Monte Carlo models were developed for the MDCT scanner to describe the x-ray source (spectra, bowtie filter, etc) and geometry factors (distance from focal spot to isocentre, source movement due to axial or helical scanning, etc). Models for the cylindrical (CTDI) phantoms were available from the previous work. For the anthropomorphic phantom, CT image data were used to create a detailed voxelized model of the phantom's geometry. Anthropomorphic phantom material compositions were provided by the manufacturer. A simulation of the physical scan was performed using the mathematical models of the scanner, phantom and specified scan parameters. Tallies were recorded at specific voxel locations corresponding to the MOSFET physical measurements. Simulations of air scans were performed to obtain normalization factors to convert results to absolute dose values. For the CTDI body (32 cm) phantom, measurements and simulation results agreed to within 3.5% across all conditions. For the anthropomorphic phantom, measured surface dose values from a contiguous axial scan showed significant variation and ranged from 8 mGy/100 mAs to 16 mGy/100 mAs. Results from helical scans of overlapping pitch (0.9375) and extended pitch (1.375) were also obtained. Comparisons between the

MOSFET measurements and the absolute dose value derived from the Monte Carlo simulations demonstrate agreement in terms of absolute dose values as well as the spatially varying characteristics. This work demonstrates the ability to extend models from a single detector scanner using cylindrical phantoms to an MDCT scanner using both cylindrical and anthropomorphic phantoms. Future work will be extended to voxelized patient models of different sizes and to other MDCT scanners.

(Some figures in this article are in colour only in the electronic version)

1. Introduction

Although computed tomography (CT) represents only a small percentage of radiological examinations, it results in a significant portion of the radiation dose received by patients from medical procedures (Shrimpton and Edyvean 1998). In addition, the introduction of multidetector CT (MDCT), with its greater coverage and faster gantry rotation times, has increased the diagnostic utility of MDCT. This in turn has led to the increasing clinical application of CT and discussion about the appropriate use of CT, specifically in its application to children and in screening populations, primarily because of the radiation dose delivered during the exam (Paterson 2001, Brenner *et al* 2001, Donnelly *et al* 2001, Feigal 2001, Brenner and Elliston 2004, Brenner 2004).

For these reasons, there continues to be motivation to develop methods to accurately estimate the absorbed radiation dose and, ultimately, the radiological risk from a CT examination. While methods to estimate radiological risk using the effective dose approach have been developed (ICRP 1991, McCollough and Schueler 2000), these require estimates of the dose to each radiosensitive organ; this is problematic in CT because of the highly localized patterns of exposure, which are characteristic of the scanning technique and which yield variable doses to different organs and because direct measurement is not possible.

Previous methods that calculate the dose to organs from CT used Monte Carlo simulation methods applied to standard mathematical phantoms (Jones and Wall 1985, Jones and Shrimpton 1991, Kramer *et al* 1982) or are derived from the results of these methods (Huda and Atherton 1996, Atherton and Huda 1996, LeHeron 1993, ImPACT 2000, Kalender *et al* 1999). Although some methods allow the user to input either axial or spiral CT scanning protocols, the dose estimates from spiral scan protocols are approximated from the contiguous axial scan data and are not derived directly from simulations of a spiral acquisition. In addition, the CT scanner models used in the original work pre-date helical CT scanners or multidetector scanners.

Several approaches have been developed to approximate the behaviour of current MDCT scanners such as those employed by ImPACT in their dose calculation spreadsheet (ImPACT 2000, Jarry *et al* 2002). To take into account the effects of patient size, some previous efforts have used Monte Carlo modelling applied to non-standard mathematical models such as a 14-year-old female (Caon *et al* 1999, 2000). Recently, Schmidt and Kalender (2002a, 2002b) developed a Monte Carlo based method to model an MDCT scanner directly. In this work, the characteristics of one MDCT (Volume Zoom, Siemens Medical Solutions, Forcheim, Germany) were modelled and results presented to demonstrate validation of these models. In addition, the model was used to demonstrate the effects of an axial (in-plane only) tube current modulation scheme (Schmidt *et al* 2003).

We previously (Jarry *et al* 2002) developed a method to estimate radiation dose from axial and spiral CT scans using a Monte Carlo modelling code where the source movement was modelled directly and the source model was applied to phantoms and a tomographic computational patient model. In that study, the source model developed was for a single detector helical CT (CT/i, GE Healthcare Systems, Waukesha, WI), which incorporated details about the x-ray source and filtration (including bowtie filter), the scanner geometry (distance from focal spot to isocentre, etc) and specifically modelled axial and helical source movement patterns. We also developed object models for standard CT dosimetry phantoms (CTDI head and body phantoms) as well as implemented the same reference man mathematical phantoms used above (Snyder *et al* 1969) and a computational tomographic model based on a real patient scan. In that study, the model was tested by directly comparing simulation results to physical measurements based on cylindrical CTDI phantoms. Indirect comparisons were also made between our simulation results and those published based on the MIRD V (using ImPACT dose calculator—www.impactscan.org). The results of that study showed excellent agreement between simulation and measurement where the CTDI phantom results agreed to within 10% across all beam energies and collimations tested. Agreement with other published results was also excellent with the MIRD V results agreeing to within 11%.

This study was designed to *extend* the verification of Monte Carlo methods for estimating CT dose from cylindrical phantoms scanned on a single detector CT scanner to the use of both cylindrical *and* physical anthropomorphic phantoms scanned on MDCT scanners. This was done by comparing physical measurements to results obtained from simulations using a detailed Monte Carlo model of MDCT. The long-term goal of this research is to create methods to accurately estimate radiation dose to individual patients undergoing CT scanning. The purpose of this study was to provide the testing and verification in well-understood physical objects before moving on to computational patient models such as those described in Jarry *et al* (2002) or the family of models developed by the GSF (Petoussi-Henss *et al* 2002, Zankl *et al* 2002).

2. Materials and methods

2.1. Overview of the Monte Carlo method

All simulations were performed using the MCNPX (MCNP eXtended v2.5.c) Monte Carlo code (Waters 2002, 2003). MCNPX is a superset of MCNP4C and supports the transport of 34 different particles. The MCNPX simulation package provides for conventional modelling based upon a combinatorial geometry system using planes, cylinders, cones and spheres to define the overall geometry. In addition, it supports macrobodies and a mesh tally feature that allows the user to overlay a Cartesian, cylindrical or spherical tally mesh over an arbitrary simulation geometry. The mesh tally feature was used extensively for this work in order to efficiently tally the dose in a high-resolution Cartesian-coordinate mesh structure. For this work, the simulation is operated in photon mode with a low-energy cutoff of 1 keV. The photon transport model creates electrons but assumes that they travel in the direction of the primary photon and that the electron energy is deposited at the photon interaction site, creating a condition of charged particle equilibrium (CPE). Under conditions of CPE, the assumption that collision kerma is equal to absorbed dose is valid and a collision-kerma tally can be used for the absorbed dose calculations. For all simulations, the collision kerma was calculated based upon a track-length estimate of the photon energy fluence. Energy fluence was converted to dose rate using the mass energy-absorption coefficients obtained by Hubbell and Seltzer (1995). In all simulations, the number of histories was selected to obtain relative errors less

than or equal to 1%. The relative error is defined as the 1σ standard deviation divided by the average tally result. For simulations involving the mesh tally, the code scores the net energy deposition from all particles traversing a mesh cell.

2.2. General CT model

2.2.1. The CT scanners. A LightSpeed Plus or a LightSpeed 16 computed tomography scanner system (General Electric Medical Systems, Waukesha, WI) was used in all simulations. The LightSpeed Plus is a third-generation multidetector CT scanner (MDCT) equipped with 16 rows of detectors, with each row being 1.25 mm wide (referenced to isocentre). The user may select x-ray beam collimations of 4 × 1.25 mm, 4 × 2.5 mm, 4 × 3.75 mm and 4 × 5 mm as well as 2 × 0.625 mm (*Note:* all beam collimations are given in the format of $N \times T$, where N represents the number of data channels and T represents the nominal width of each data channel; each data channel may represent $\geqslant$1 detector row). The system supports nominal beam energies of 80, 100, 120 or 140 kVp. The scanner operates in both axial and helical modes; in the helical mode, the pitch (using IEC definition of pitch, International Electrotechnical Commission 2002) is restricted to values of 0.75 and 1.5. These are referred to by the manufacturer as HQ and HS pitch values, respectively. The scanner is equipped with x-ray beam filtration that includes both head and body bowtie filters, which are used to compensate for the variation in body thickness across the transverse sections of the body. The distance from the focal spot to the isocentre is 54 cm and the distance from the focal spot to the detector is 95 cm. The fan beam is collimated in the x–y plane to a fan angle of 55°.

The LightSpeed 16 is also a third-generation MDCT, with a different detector design and different pitch values. This scanner has 16 rows of 0.625 mm wide detectors as well as eight rows of 1.25 mm detectors. Therefore, it offers the user the following x-ray beam collimation options: 16 × 0.625 mm (8 × 1.25 mm), 16 × 1.25 mm (8 × 2.5 mm) as well as 2 × 0.625 mm and 1 × 5 mm modes. For helical scans, it allows pitches of 0.625, 0.875, 1.35 and 1.675 in the 8-channel mode and 0.5625, 0.9375, 1.375 and 1.75 in the 16-channel mode. The beam energies and geometry and filtration options are the same as the LightSpeed Plus.

2.3. Modelling of the CT source: source geometry and movement

As was done in our previous work (Jarry *et al* 2002), modifications to the standard MCNP source code were implemented to allow the simulation of the scanner and its operation for various scan protocols. MCNP requires that the spatial coordinates, the direction vector and the energy of the emitted particle be specified. The source was modelled so that single axial scans, contiguous axial scans and helical scan protocols of arbitrary pitch could be simulated. The source model assumes that the photons are emitted from a point at the location of the x-ray tube anode. The source energy spectra were obtained from the manufacturer for all available kVps and were implemented in the MCNP code as look-up tables. Information about both internal and external filtration (head and body bowtie filters) was also provided by the manufacturer. The effects of these filters were modelled using the same approach to calculating weight factors based on attenuation coefficients that was described in Jarry *et al* (2002).

2.4. Object models

2.4.1. The CTDI simulation. In this work, the standard body CTDI dosimetry phantom was used to perform measurements. This cylindrical phantom is 15 cm in length with a

diameter of 32 cm. It is made of polymethylmethacrylate (PMMA) and has five sockets that will accept a PMMA insert or the pencil ion chamber. A mathematical model of this phantom was previously developed in Jarry *et al* (2002). The pencil ion chamber used to measure exposure as part of the CTDI measurement was a Radcal 10 × 5–3CT and the corresponding electrometer was a Radcal Radiation Monitor, model 1515 (Radcal Corporation, Monrovia, CA). The walls and the electrode of the ion chamber are made of C552 air equivalent material. The chamber is surrounded by a polyacetal cap. The active volume is 0.3 cm^3 over an active length of 10 cm. The ion chamber was explicitly modelled as three concentric cylinders to model the electrode, the chamber wall and the air space in between.

2.4.2. Physical anthropomorphic phantom. In the previous work, a mathematical anthropomorphic model (Snyder *et al* 1969) was used in the simulations; in this work, a physical anthropomorphic model was used for both measurement and simulations. The ATOM family adult male (CIRS, Norfolk, VA, http://www.cirsinc.com/products/pdf/model_atomfamily.pdf) was used in all measurements. This physical phantom represents the head and torso (the phantom does not have legs) of a standard man having dimensions of 173 cm height and 73 kg weight. The phantom has materials that model bone, soft tissue, lung and spinal cord tissues. The manufacturer provides information about the density and composition of each simulated tissue type.

2.4.3. Computational tomographic model—anthropomorphic phantom. Using the approach described in DeMarco *et al* (1998), a simulation model was created based on the physical anthropomorphic phantom. This first required that a CT scan be obtained of the phantom using the LightSpeed Plus described above. The image data obtained were contiguous axial scans, reconstructed with 5 mm thickness and a voxel size of 0.742 mm × 0.742 mm. The resulting image data were used to convert the CT image data into a computational tomographic model. A look-up table was created to convert each voxel's Hounsfield number to a Monte Carlo material index based upon the five tissue types present within the phantom. The result is a voxelized model of the anthropomorphic phantom in which each voxel is described by its location as well as its tissue type.

2.4.4. Surface dosimetry on the phantoms—MOSFETs. To obtain spatially sensitive dosimetry measurements on the surface of the phantoms, MOSFET (metal oxide semiconductor field effect transistor) detectors were employed (Peet and Pryor 1999, Bower and Hintenlang 1998). The MOSFETs used were model TN 1002RD (Thomson-Nielsen, Ottawa, ON, http://www.thomson-elec.com/downloadables/tech7.01.pdf) with an active area of 0.1 mm^2. In the measurements performed, 20 detectors were used, with each group of 5 being connected to a common bias supply. To minimize the beam entry angle bias, the detectors were positioned with their bulb side away from the surface of the phantom and were placed so that the x-ray beam would primarily enter perpendicular to the direction of the leads. These MOSFET measurements were made primarily to obtain profiles along the longitudinal (z) axis and so the detectors were placed at approximately 1.6 mm intervals along that axis. To reduce any influence of scattered radiation between MOSFETs, the detectors were also placed with an offset in the x direction (medial–lateral direction) as well. The arrangement of the MOSFETs is described in the diagram of figure 1. Figures 2 and 3 are photographs of this arrangement placed on the surface of the body CTDI and anthropomorphic phantoms, respectively.

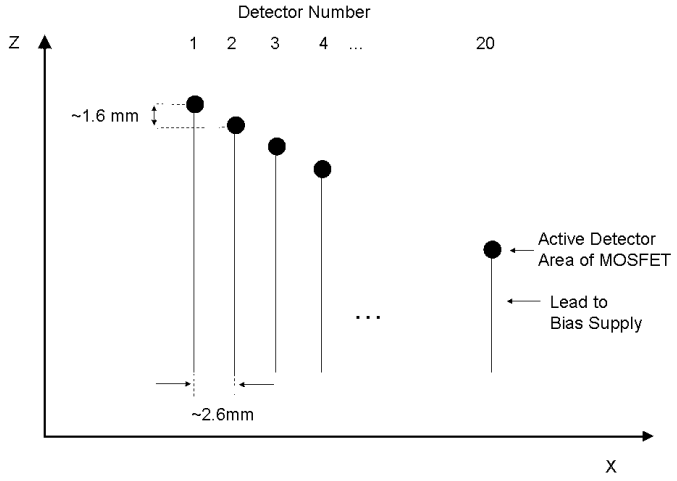

Figure 1. Diagram describing the arrangement of the 20 MOSFET detectors. Perspective is from an overhead view. Centre-to-centre spacing of the MOSFETs is approximately 1.6 mm along the z (longitudinal) axis and 2.6 mm along the x-axis. MOSFET detectors are offset in both z (longitudinal) and x (medial–lateral) directions so that scatter between detectors was minimized.

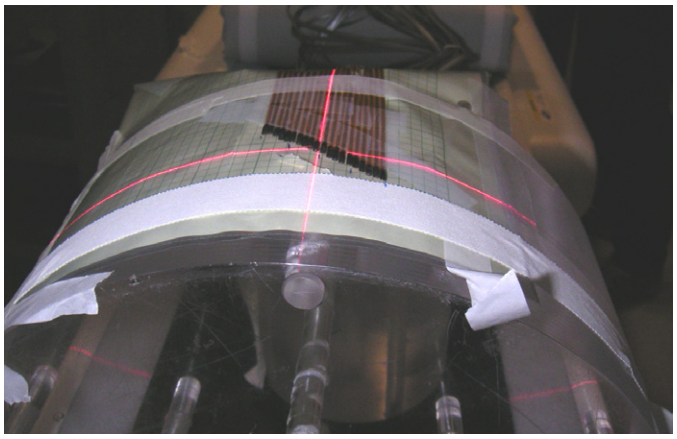

Figure 2. Photograph of MOSFET layout on surface of the body (32 cm diameter) CTDI phantom. View is from inside the CT gantry looking back towards the CT table.

2.5. Experiments

2.5.1. The normalization and validation measurements. The normalization and validation scans that were described in the earlier work of Jarry *et al* (2002) were repeated on the MDCT LightSpeed Plus. Thus, two sets of measurements were acquired using the Radcal pencil ionization chamber. The first set of measurements was used to compute the normalization factors that would allow conversion from simulation results to absolute dose values. To do this, single axial scan (one full rotation) exposures were acquired in air at the scanner isocentre for all of the available beam energies of 80, 100, 120 and 140 kVp using a 4 × 5 mm (20 mm total) beam collimation and the body bowtie filter. The tube current was kept constant at 100 mA and the rotation time was set to 1 s.

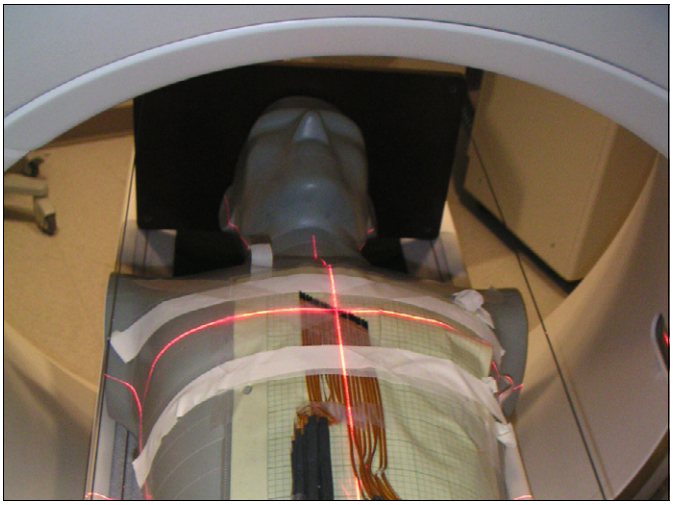

Figure 3. Illustration of MOSFET layout on the central anterior chest surface of the adult male anthropomorphic phantom on a CT scanner table. Again, MOSFET detectors are offset in both z (longitudinal) and x (medial–lateral) directions so that scatter between detectors was minimized. Care was taken to position the MOSFETs as close to the chest as possible.

The second set of measurements was obtained using the CTDI body dosimetry phantom and was used for comparison with the simulation results. For this set, the air kerma was measured in the body CTDI phantom. Ion chamber measurements were obtained at the centre and at the 12:00 peripheral position. The 12:00 chamber position with respect to this study represents the most anterior chamber location directly above the centre chamber position and lies on the periphery of the phantom at a distance of 1.0 cm from the surface. These measurements were obtained under the same conditions used for the normalization measurements, i.e. a single axial scan using 100 mAs and the above-described beam collimation, energies and bowtie filter selection. All exposures were obtained using the 100 mm pencil ion chamber and then were converted to the standard computed tomography dose index ($CTDI_{100}$) value using the approach described in the European Guidelines (2002).

2.5.2. Simulation of the CTDI phantoms for normalization and comparison purposes. In order to compare the Monte Carlo simulation results to the physical measurements made above, the analogous simulations were performed. For the normalization simulations, single axial scans were simulated in air at the scanner isocentre for beam energies of 80, 100, 120 and 140 kVp using the 20 mm (4×5 mm) beam collimation with the body bowtie filter. For each simulation, the result was the Monte Carlo calculated air kerma (mGy per source particle started) that occurred in the simulated ion chamber. The air-kerma result was computed by scoring the photon energy fluence and multiplying by the energy-dependent mass energy-absorption coefficient for air.

For the validation experiments, simulations were performed for the body CTDI acrylic phantom under the same conditions used for the normalization measurements, i.e. a single axial scan using 100 mAs, body bowtie filter and the slice thicknesses and energies described above. Measurements were simulated so that air-kerma values were obtained at the centre and at the 12:00 peripheral position of the CTDI phantom. Note that for each simulation, the pencil ionization chamber was included in the simulations as well. The MOSFET detectors

Table 1. Normalization factors for converting the Monte Carlo simulation results from mGy per source particle to mGy/100 mAs for the LightSpeed Plus MDCT scanner. The per cent relative error for the MCNPX results is less than 0.5%. The pencil chamber measurements and MCNPX simulations were performed in air using the body bowtie filter. Normalization differences are less than 0.5% between the body and head bowtie filter.

kVp	Beam collimation (mm)	Pencil chamber (mGy/100 mAs)	Monte Carlo (mGy/part)	Normalization factor (part/100 mAs)
80	4 × 5	8.10	1.94×10^{-13}	4.18×10^{13}
100	4 × 5	14.70	2.52×10^{-13}	5.83×10^{13}
120	4 × 5	22.71	2.97×10^{-13}	7.65×10^{13}
140	4 × 5	31.93	3.36×10^{-13}	9.50×10^{13}

were not explicitly modelled when comparing the air-kerma variation along the surface of the CTDI body phantom. Using the cylindrical geometry of the CTDI phantom, the air-kerma tally was performed in a cylindrical annulus at the surface of the phantom with an annulus thickness of 2 mm and a longitudinal spacing of 2 mm.

2.5.3. Monte Carlo normalization factor. Because the MCNP code calculates the dose or exposure per unit source particle and does not take into account the fluence changes when varying the beam collimation, all simulation results must be normalized in order to obtain absolute dose or exposure. The normalization factor described previously (Jarry *et al* 2002) is also used in this study and described here by equation (1) with units of source particle per mAs and is a function of both beam energy E and beam collimation NT:

$$(\mathrm{NF})_{E,\mathrm{NT}} = \frac{(D_{\mathrm{air,measured\,per\,mAs}})_{E,\mathrm{NT}}}{(D_{\mathrm{air,simulated\,per\,particle}})_{E,\mathrm{NT}}}, \tag{1}$$

where $D_{\mathrm{air,simulated}}$ is the air kerma found by simulating the ion chamber at the scanner isocentre at beam energy E and beam collimation NT and $D_{\mathrm{air,measured}}$ is the air kerma measured in air at the scanner isocentre. Because the normalization factor is given on a per mAs basis, the simulation results are multiplied by the normalization factor and the total mAs to obtain absolute dose. In the case of a contiguous axial or helical protocol, the total mAs is equal to the mAs per rotation times the number of rotations. For helical scans, the number of rotations is affected by pitch; larger pitch values for a given coverage mean fewer rotations and vice versa. Equation (2) is used to obtain the absolute dose from the simulated data:

$$(D_{\mathrm{absolute}})_{E,\mathrm{NT}} = (D_{\mathrm{simulated}})_{E,\mathrm{NT}} \times (\mathrm{NF})_{E,\mathrm{NT}} \times \frac{\mathrm{mAs}}{\mathrm{rotation}} \times \#\,\mathrm{rotation}. \tag{2}$$

The simulated dose is calculated based upon an energy fluence tally and the mass energy-absorption coefficients for the appropriate material. Normalization factors were obtained for each beam energy used and one beam collimation setting (4 × 5 mm = 20 mm). Table 1 lists the normalization factors as a function of kVp for the LightSpeed Plus using 4 × 5 mm beam collimation and the body bowtie filter.

2.5.4. MOSFET measurements and normalization. As an intermediate comparison step between single axial scans in cylindrical phantoms and scans through an anthropomorphic phantom, we used contiguous axial scans through the entire extent of the cylindrical phantoms as a basis of comparison between measurement and simulation results. Because a pencil ionization chamber would not be able to capture the spatial variations along the z-axis, the MOSFET detectors were used.

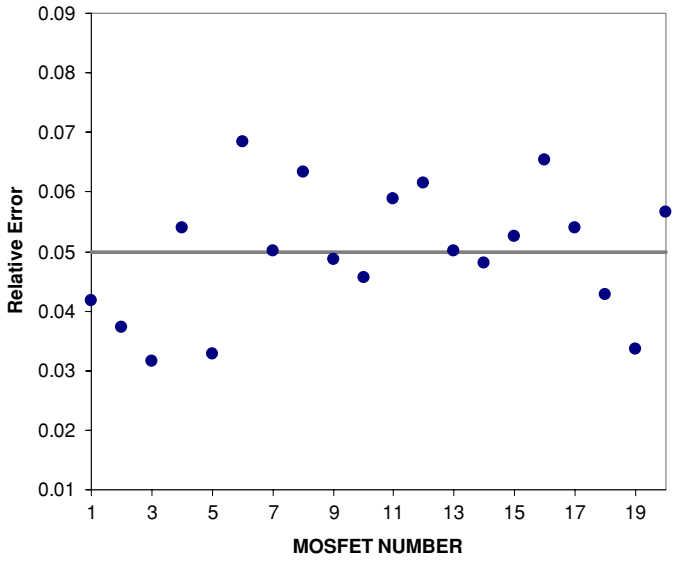

Figure 4. The reproducibility of in-air MOSFET readings based upon a standard bias setting and ten readings per detector. The scan parameters for each reading were identical and based upon a scanner nominal beam collimation of 4 × 5 mm, 120 kVp, 240 mA and 1 s rotation time. The average relative error for the 20 MOSFET detectors is 0.05. The relative error is defined as the standard deviation divided by the mean.

Measurements and normalization calculations for the MOSFETs were performed on the LightSpeed 16. First, the MOSFETs were exposed in air at isocentre under the same conditions as the pencil ionization chamber above (120 kVp, 4 × 5 mm beam collimation, body bowtie, 100 mAs). For each in-air measurement, a MOSFET detector was placed at isocentre and the corresponding pencil ionization chamber measurement was used to create a calibration factor based upon the ratio of the pencil-chamber reading versus the MOSFET signal with units of cGy per mV per mAs. The cGy unit represents the air-kerma dose as measured by the pencil chamber. Figure 4 illustrates the MOSFET signal reproducibility for 20 different detectors. The per cent relative error over the 20-detector group was 5% based upon ten measurements per detector.

Following these calibration measurements, the following test scans were performed: (1) a single axial scan at one z-axis location, (2) a contiguous axial scan through the extent of the body CTDI phantom and (3) helical scans of two different pitch values (0.9375 and 1.375) through the extent of the body CTDI phantom. In each case, the MOSFETs were placed on the surface of the phantom (as illustrated in figure 2). The reading of each MOSFET was recorded, specifically noting the position of each MOSFET. For all of these scans, the technical parameters were 120 kVp, 4 × 5 mm beam collimation and 1 s rotation time. The mA setting for the single axial scan was 240, and it was 440 mA in all of the other scans that went through the extent of the phantom.

Simulations were performed using the identical set of scan parameters with a voxelized model of the body CTDI phantom to evaluate the spatially varying results. Results from normalization measurements were used to obtain absolute dose values. The air kerma was scored along the surface of the body CTDI phantom for comparison with the MOSFET results. In addition, because the simulation can score dose in each voxel of the phantom model, the

Table 2. Comparison of measured and simulated results from a single axial scan in the CTDI body phantom using the LightSpeed Plus scanner at each kVp setting; all scans using 100 mA, 1 s scan, 4 × 5 mm beam collimation, body bowtie filter.

kVp	Position	Pencil chamber (mGy/100 mAs)	Monte Carlo (mGy/100 mAs)	% Difference
80	Centre	1.34	1.29	−3.4
	12	3.45	3.37	−2.2
100	Centre	2.97	2.89	−2.5
	12	6.66	6.53	−1.8
120	Centre	5.12	4.95	−3.4
	12	10.48	10.28	−2.0
140	Centre	7.65	7.51	−1.8
	12	15.01	14.63	−2.5

variation along any direction and at any position within the phantom could be obtained. In this case, we obtained results within both the axial and sagittal planes of the phantom to demonstrate the spatial variations of the dose distribution within the phantom.

2.5.5. Contiguous axial scans in a heterogeneous anthropomorphic phantom. The final comparison between measurement and simulation was based on surface measurements from contiguous axial scans using the anthropomorphic phantom described above. Contiguous axial scans were acquired through the thorax of the adult male phantom using the LightSpeed 16 scanner with 120 kVp, 4 × 5 mm beam collimation, 100 mA, 1 s rotation time and the body bowtie filter. The MOSFETs described above were placed on the central anterior surface of the phantom, as illustrated in figure 3, and the reading of each MOSFET was recorded, specifically noting its position. Care was taken to position the MOSFET detectors as closely as possible to the surface of the phantom. Simulations were obtained under identical conditions using the LightSpeed 16 scanner model and the voxelized model of the anthropomorphic phantom. The position of the MOSFET detectors was obtained by examining the image data. Again, because the simulation can tally dose in each voxel of the phantom model, the variation along any direction and at any position within the phantom could be obtained. In this case, we obtained results within both the axial and sagittal planes of the phantom to demonstrate the spatial variations of the dose distribution within the phantom. The MOSFET detector values from the surface measurements and the corresponding simulation values were compared on a qualitative basis by plotting each resulting profile.

3. Results

Results from the comparison between pencil ion chamber based measurements using the CTDI body phantom measurements and the absolute values obtained from the simulation model are shown in table 2. These results show excellent agreement with a maximum per cent difference of 3.4% for all values tested. The comparison between MOSFET measurements and Monte Carlo simulations from a single axial scan of the CTDI body phantom is illustrated in figure 5. The error bars reflect the uncertainty in the axial direction (z-axis) from MOSFET placement and in the dose direction due to MOSFET output variability. The MOSFET detectors were staggered on the surface of the CTDI body phantom as illustrated in figure 2. There is good agreement between the two sets of values with the Monte Carlo simulation slightly

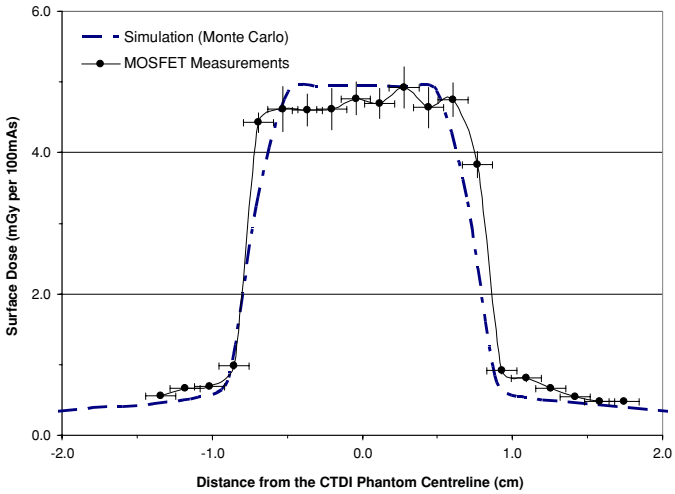

Figure 5. Results showing comparison of MOSFET measurement and corresponding Monte Carlo simulation results of a single axial scan surface air-kerma distribution profile along the z direction for a body phantom scanned using 120 kVp and 4 $\times$ 5 mm beam collimation. The Monte Carlo results are based upon a per cent relative error of less than 2% for all data points and are not shown for clarity. The MOSFET measurements are presented with a y-axis, relative error based upon the reproducibility results of figure 4 and an x-axis uncertainty based upon an approximate positioning error of ± 1 mm relative to its adjacent neighbour(s).

underestimating the air-kerma profile in the plateau and through the tail of the penumbral region. The Monte Carlo results simulate the actual air-kerma profile along the surface of the phantom and are not explicitly modelling the MOSFET detectors. The observed profile differences could also be due to the simplistic CT source model used for this study, with photons emitted from a point source and nominal collimation. In reality, the CT source has a finite focal spot size with scatter contributions from the collimation assembly and tube housing. The effect of these realistic source parameters remain a topic for future study.

Results from the contiguous axial scans through the CTDI body phantom are illustrated in figure 6(a) and shows the comparison of the measured MOSFET values obtained at the surface of the phantom to those obtained by simulation. Both the measured and simulated results demonstrate the spatial variation of dose at the surface of the phantom that results even when a contiguous axial scan is performed. Both measured and simulated results demonstrate approximately the same degree of variation from peak to trough with approximately the same period of variation. It should also be noted that the results from the Monte Carlo simulations are much smoother as they represent ideal detectors, do not reflect any inter-detector variations and can be obtained at a very large number of sample points rather than the limit of 20 MOSFET detectors we have for the physical measurements. Results from helical scans of pitch 1.375 and pitch 0.9375 are shown in figures 6(b) and (c), respectively. These curves show the comparison between the measured and simulated air-kerma profiles at the surface of the body CTDI phantom. These results again demonstrate good agreement between the measured and simulated values, this time under helical scan conditions. It should be noted that in all three conditions (contiguous axial, overlapping helical and extended helical scan) the variation of surface dose magnitude is nearly a factor of 2 for the CTDI body phantom.

The results from the heterogeneous anthropomorphic phantom are shown in figures 7(a)–(c). The figures illustrate a profile of the MOSFET detector measurements made at the anterior

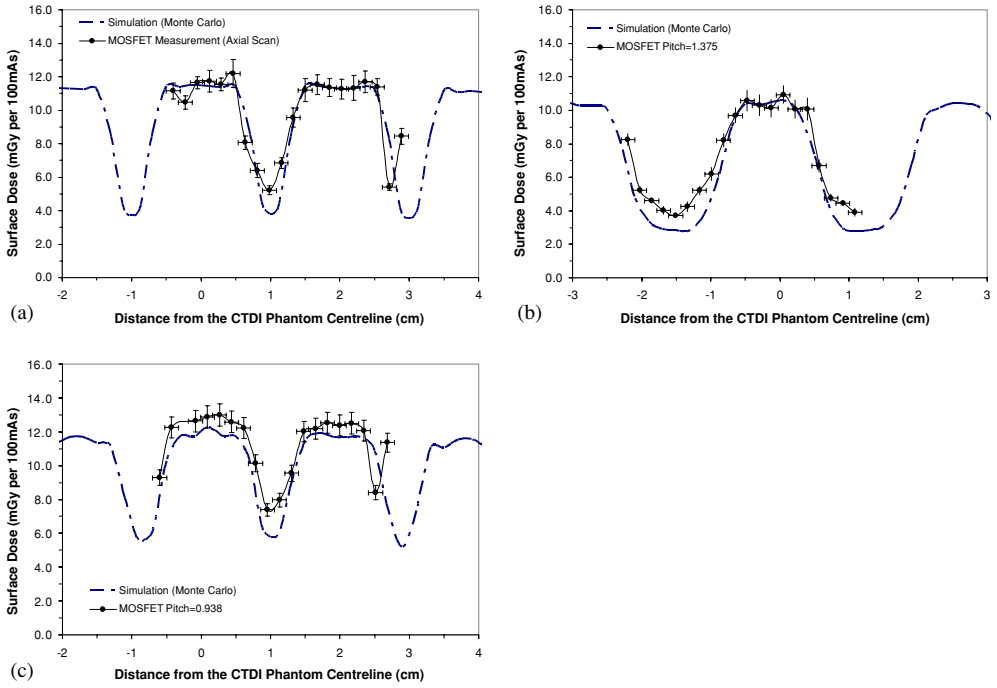

Figure 6. Comparison of measured and simulated surface dose measurements along the longitudinal axis of the body CTDI phantom resulting from (a) contiguous axial scan, (b) helical scan, pitch = 1.375 and (c) helical scan, pitch = 0.9375. The Monte Carlo results are based upon a per cent relative error of less than 2% for all data points. The MOSFET measurements are presented with a *y*-axis, relative error based upon the reproducibility results of figure 4 and an *x*-axis uncertainty based upon an approximate positioning error of ±1 mm relative to its adjacent neighbour(s).

chest surface of the phantom for a contiguous axial scan, and helical scan pitch = 1.375 and 0.9375, respectively. It also shows the results of the simulation under the same scan conditions using the voxelized model of the anthropomorphic phantom. This figure demonstrates surface dose variations that are very similar to those observed in the cylindrical phantoms, despite the heterogeneous shape and composition of this phantom. These figures also demonstrate variations in surface dose that range from at least 50% for the overlapping pitch (pitch 0.9375) to more than 2.0 for the extended pitch (pitch 1.375). These figures also demonstrate that the magnitude of the surface dose is higher than that observed for the CTDI body phantom in figure 6. This is not surprising as the anthropomorphic phantom is less than 32 cm diameter in the locations where these measurements were made.

4. Discussion

In this manuscript we have extended the modelling approach for estimating radiation dose to a multidetector CT (MDCT) scanner including the x-ray spectra, filtration and geometry of the MDCT scanner. The simulation model also included a voxelized model of the cylindrical body phantom as well as a voxelized model of a heterogeneous anthropomorphic phantom.

This model was tested under a variety of conditions by comparing measured values to those obtained from simulations and applying the normalizations to obtain absolute dose

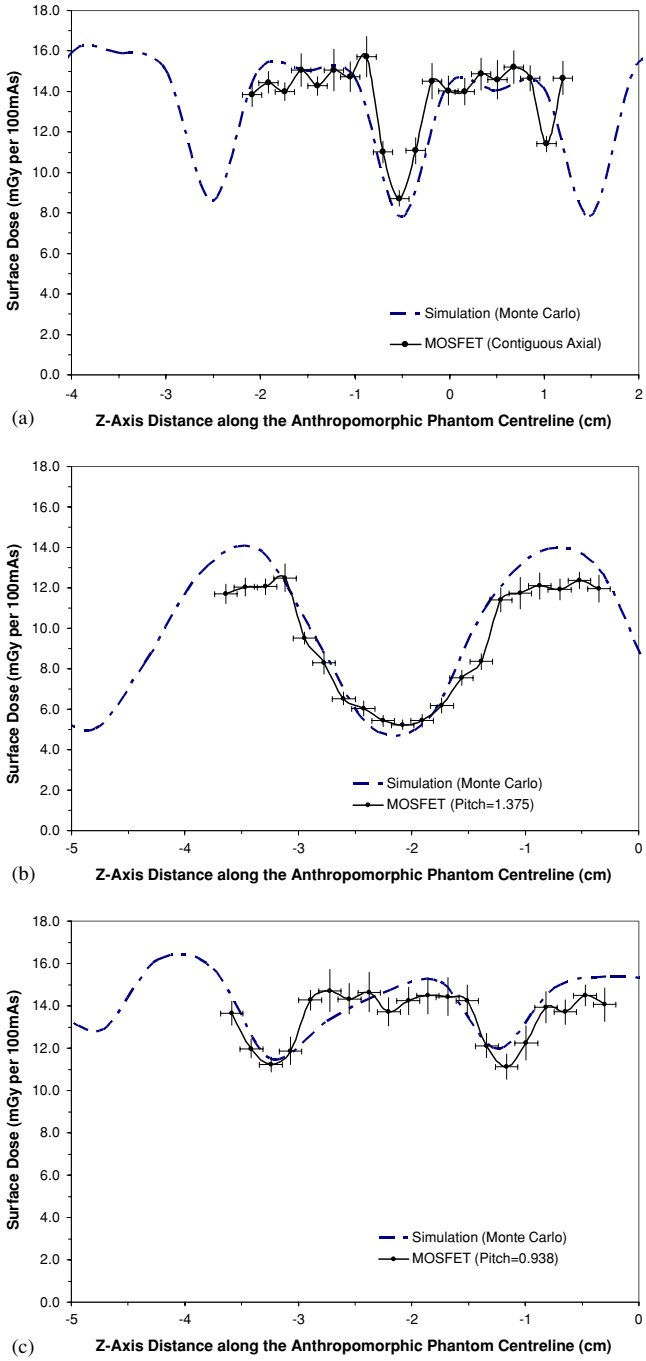

Figure 7. Comparison of measured and simulated anterior chest surface dose measurements along the z-axis of the anthropomorphic phantom resulting from (a) contiguous axial scan, (b) helical scan, pitch $= 1.375$ and (c) helical scan, pitch $= 0.9375$ through the extent of the body CTDI phantom. The Monte Carlo results are based upon a per cent relative error of less than 2% for all data points. The MOSFET measurements are presented with a y-axis, relative error based upon the reproducibility results of figure 4 and an x-axis uncertainty based upon an approximate positioning error of ± 1 mm relative to its adjacent neighbour(s).

values. Experiments using the homogeneous, cylindrical CTDI body phantom scanned with a single axial exposure, showed excellent agreement between measured and simulated values, with all values across all conditions and positions agreeing to within 3.4%. One reason for the good agreement in this effort was that the spectral data were obtained from the manufacturer, rather than estimating from the Boone spectra (Boone and Seibert 1997) as in the previously published effort. The data suggest a slight systematic underestimate of the Monte Carlo simulated dose values versus measurement. For this study, the table was modelled as a flat carbon slab with a thickness approximately matched to the true table thickness as measured from an actual CT scan. In reality, the table is a composite geometry of carbon fibre of unknown density and air space.

The next test condition was based upon different scans through the body CTDI phantom where surface dose values were obtained using MOSFET detectors for measurements. Both measured and simulated values demonstrate good agreement for the surface dose that resulted from a single axial scan, contiguous axial scans, overlapping helical scans (pitch <1) and extended helical scans (pitch >1). The variations in surface dose from contiguous axial scans (and overlapping pitch scans) were larger than originally expected, with values of a factor of least 2.0 being observed at each scan condition. It does appear that these variations are due to a combination of (a) the slight divergence of the beam in the longitudinal direction, (b) the intersection of the beam with the surface of the phantom at 16 cm from isocentre and (c) at the surface of the CTDI body phantom, the majority of exposure is due to entrance exposure (exposure originating at other source angles is attenuated by up to 32 cm of PMMA). The resulting variations at the surface were also observed in the Monte Carlo simulations and the agreement between the measured and simulated values was good with both demonstrating similar magnitudes and spatial extent of the variations.

The final test conditions described in this manuscript were scans through the thorax of an anthropomorphic phantom where MOSFET detectors were placed on the anterior chest surface of the phantom. Results from both measured values and simulations demonstrate that the distribution of dose is complex and varies in the x, y and z directions. We were able to demonstrate good agreement between the measured and simulated values obtained at the position of the MOSFETs. In addition, the patterns for the contiguous axial scans in CTDI body and anthropomorphic phantoms were similar in terms of their shape variations and periodicity. Finally, the results demonstrated that the absolute value of surface dose was higher in the anthropomorphic phantom by about 50% versus the body CTDI phantom; this was expected due to the difference in diameter and attenuation of the two phantoms. In general, figures 6 and 7 also illustrate a systematic overestimation of the dose variation along the phantom surface for the Monte Carlo simulations relative to the MOSFET measurements. As described previously, this effect could be explained by the simplistic source model and the dose contribution from focal spot source size and tube scatter effects. Future analysis will require detailed drawings of the tube housing and collimation assembly in order to evaluate this discrepancy.

5. Conclusion

This work has shown that the radiation dose patterns in CT can be complex, even for contiguous axial scans in homogeneous phantoms. To obtain accurate results from simulations, detailed models must be employed to accurately capture these variations. Results in this work from both cylindrical and anthropomorphic phantoms demonstrate that the models developed for MDCT yield very accurate results and are very encouraging. Future work includes extending the analysis to other sets of technical factors (different pitch values—only two were tested

here; different beam widths, etc). We have also begun implementing patient model objects. Specifically, the GSF patient model family of adult and child models (Petoussi-Henss *et al* 2002, Zankl *et al* 2002) is being implemented and tested. These are voxelized models of humans based on CT scan image data and where the location and composition of radiosensitive organs are already determined. This will allow the simulation of an MDCT scan (e.g. chest scan, abdomen scan, etc) on a patient where the radiation dose in each organ could be tallied. This would allow estimation of dose from each type of scan (chest, abdomen, etc) to a certain patient model under different scan conditions (such as different parameter selections such as pitch, kVp). Because these models represent patients of different size, the effects of size on the complex dose distribution pattern can be assessed directly. Finally, we are also extending the source models to incorporate scanners from other manufacturers and other models. In doing so, we will be able to obtain patient dose estimates from different size patients, from different scanners and different scan parameters.

References

Atherton J V and Huda W 1996 Energy imparted and effective doses in computed tomography *Med. Phys.* **23** 735–41

Boone J M and Seibert J 1997 An accurate method for computer-generating tungsten anode x-ray spectra from 30 to 140 kV *Med. Phys.* **24** 1661–70

Bower M W and Hintenlang D E 1998 The characterization of a commercial MOSFET dosimeter system for use in diagnostic x-ray *Health Phys.* **75** 197–204

Brenner D J 2004 Radiation risks potentially associated with low-dose CT screening of adult smokers for lung cancer *Radiology* **231** 440–5

Brenner D J and Elliston C D 2004 Estimated radiation risks potentially associated with full-body CT screening *Radiology* **232** 735–8

Brenner D J, Elliston C D, Hall E J and Berdon W E 2001 Estimated risks of radiation-induced fatal cancer from pediatric CT *Am. J. Roentgenol.* **176** 289–96

Caon M, Bibbo G and Pattison J 1999 An EGS4-ready tomographic computational model of a 14-year-old female torso for calculating organ doses from CT examinations *Phys. Med. Biol.* **44** 2213–25

Caon P, Bibbo G and Pattison J 2000 Monte Carlo calculated effective dose to teenage girls from computed tomography examinations *Radiat. Prot. Dosim.* **90** 445–8

DeMarco J J, Solberg T D and Smathers J B 1998 A CT-based Monte Carlo dosimetry tool for radiotherapy treatment planning and analysis *Med. Phys.* **25** 1–11

Donnelly L F *et al* 2001 Perspective. Minimizing radiation dose for pediatric body applications of single-detector helical CT: strategies at a large children's hospital *Am. J. Roentgenol.* **176** 304–6

European Guidelines on Quality Criteria for Computed Tomography (EUR 16262 EN, May 1999) 2002 Available at www.drs.dk/guidelines/ct/quality/index.htm (accessed July 2002)

Feigal D W 2001 *FDA Public Health Notification: Reducing Radiation Risk from Computed Tomography for Pediatric and Small Adult Patients* (Center for Devices and Radiological Health, Food and Drug Administration) Available at http://www.fda.gov/cdrh/safety/110201-ct.html (accessed November 2001)

Hubbell J H and Seltzer S M 1995 *Tables of X-Ray Mass Absorption Coefficients and Mass Energy-Absorption Coefficients (Version 1.03)* (online) (Gaithersburg, MD: National Institute of Standards and Technology) Available at http://physics.nist.gov

Huda W and Atherton J 1996 Energy imparted in computed tomography *Med. Phys.* **22** 1263–9

ICRP 1991 Recommendations of the International Commission on Radiological Protection *ICRP Publication 60 (Ann. ICRP* **21***)*

ImPACT Q 2000 *Imaging Performance Assessment of CT Scanners: A Medical Devices Agency Evaluation Group. CT Scanner Matching Data, Tables of CTDI Values in Air, $CTDI_w$, and Phantom Factor Values* ImPACT Internet homepage http://www.impactscan.org (status August 2000)

International Electrotechnical Commission 2002 Medical Electrical Equipment: Part 2-44. Particular Requirements for the Safety of X-Ray Equipment for Computed Tomography *IEC Publication* 60601-2-44

Jarry G, DeMarco J J and McNitt-Gray M F 2002 Monte Carlo dose verification of a commercial CT scanner with applications for patient specific dosimetry *Med. Phys.* **29** 1344

Jones D G and Wall B F 1985 Organ doses from medical x-ray examinations calculated using Monte Carlo techniques *National Radiological Protection Board* NRPB R-186

Jones D G and Shrimpton P C 1991 Survey of the practice in the UK: Part 3. Normalized organ doses calculated using Monte Carlo techniques *National Radiological Protection Board* NRPB R-250

Kalender W A, Schmidt B, Zankl M and Schmidt M 1999 A PC program for estimating organ dose and effective dose values in computed tomography *Eur. Radiol*. **9** 555–62

Kramer R, Zankl M, Williams G and Drexler G 1982 The calculation of dose from external photon exposures using reference human phantoms and Monte Carlo methods: Part I. The male (Adam) and female (Eva) adult mathematical phantoms. *GSF Report* (Germany: S-885 Neuherberg)

LeHeron J C 1993 *CTDOSE—A Computer Program to Enable the Calculation of Organ Dose and Dose Indices for CT Examinations* (Christchurch: New Zealand: Ministry of Health, National Radiation Laboratory)

McCollough C M and Schueler B A 2000 Calculation of effective dose *Med. Phys*. **27** 838–44

Paterson A, Frush D P and Donnelly L F 2001 Helical CT of the body: are settings adjusted for pediatric patients? *Am. J. Roentgenol*. **176** 297–301

Peet D J and Pryor M D 1999 Evaluation of a MOSFET radiation sensor for the measurement of entrance surface dose in diagnostic radiology *Br. J. Radiol*. **72** 562–8

Petoussi-Henss N, Zankl M, Fill U and Regulla D 2002 The GSF family of voxel phantoms *Phys. Med. Biol*. **47** 89–106

Schmidt B and Kalender W A 2002a A fast voxel-based Monte Carlo method for scanner- and patient-specific dose calculations in computed tomography *Phys. Med.* **XVIII** 43–53

Schmidt B and Kalender W A 2002b Phantom- and patient-specific dose calculations for CT *Radiology* **225** 592

Schmidt B, Leidecker C, Schaller S and Kalender W 2003 Evaluation of dose reduction by risk organ-dependent tube current modulation *Radiology* **229** 516

Shrimpton P C and Edyvean S 1998 CT scanner dosimetry *Br. J. Radiol* **71** 1–3

Shrimpton P C and Jones D G 1993 Normalised organ doses for x-ray computed tomography calculated using Monte Carlo techniques and a mathematical anthropomorphic phantom *Radiat. Prot. Dosim* **49** 241–3

Snyder W S, Fisher H L, Ford M R and Warnet G C 1969 Estimates of absorbed fractions for monoenergetic photon sources uniformly distributed in various organs of a heterogeneous phantom *J. Nucl. Med*. **3** 7–52

Waters L (ed) 2002 MCNPX User's Manual, Version 2.4.0 *Los Alamos National Laboratory Report* LA-CP-02-408

Waters L (ed) 2003 MCNPX Version 2.5.C *Los Alamos National Laboratory Report* LA-UR-03-2202

Zankl M, Fill U, Petoussi-Henss N and Regulla D 2002 Organ dose conversion coefficients for external photon irradiation of male and female voxel models *Phys. Med. Biol*. **47** 2367–85